

In-situ measured spectral directional emissivity of snow and ice in the 8–14 μm atmospheric window

Masahiro Hori ^{a,*}, Teruo Aoki ^b, Tomonori Tanikawa ^c, Hiroki Motoyoshi ^d, Akihiro Hachikubo ^e,
Konosuke Sugiura ^f, Teppei J. Yasunari ^g, Hans Eide ^h, Rune Stordvold ⁱ, Yukinori Nakajima ^j,
Fumihiko Takahashi ^k

^a EORC/Japan Aerospace Exploration Agency, 1-8-10 Harumi, Chuo-ku, Tokyo 104-6023, Japan

^b Meteorological Research Institute, 1-1 Nagamine, Tsukuba, Ibaraki 305-0052, Japan

^c Department of Civil Engineering, Kitami Institute of Technology, 165 Koencho, Kitami 090-8507, Japan

^d Department of Polar Science, The Graduate University for Advanced Studies (Sokendai) 1-9-10 Kaga, Itabashi-ku, Tokyo, 173-8515, Japan

^e New Energy Resources Center, Kitami Institute of Technology, 165 Koencho, Kitami 090-8507, Japan

^f IORGC/Japan Agency for Marine-Earth Science and Technology, 2-15 Natsushima-chou, Yokosuka 237-0061, Japan

^g Division of Geoscience, Environmental Earth Science, Hokkaido University, Kita-ku, Sapporo 060-0819, Japan

^h Stevens Institute of Technology, Hoboken, Castle Point on Hudson, NJ 07030, USA

ⁱ NORUT Information Technology Ltd., POB 6136, 9294 Tromso, Norway

^j Ministry of Education, Culture, Sports, Science and Technology, 2-5-1 Marunouchi, Chiyoda-ku, Tokyo 100-8959, Japan

^k Remote Sensing Technology Center of Japan, 1-8-10 Harumi, Chuo-ku, Tokyo 104-6021, Japan

Received 22 August 2005; received in revised form 1 November 2005; accepted 5 November 2005

Abstract

The directional emissivity of snow and ice surfaces in the 8–14 μm thermal infrared (TIR) atmospheric window was determined from spectral radiances obtained by field measurements using a portable Fourier transform infrared spectrometer in conjunction with snow pit work. The dependence of the directional emissivity on the surface snow type (grain size and shape) was examined. We obtained emissivity spectra for five different surface types, i.e., fine dendrite snow, medium granular snow, coarse grain snow, welded sun crust snow, and smooth bare ice. The derived emissivities show a distinct spectral contrast at wavelengths $\lambda = 10.5\text{--}12.5\ \mu\text{m}$ which is enhanced with increasing the snow grain size. For example, emissivities at both 10.5 μm and 12.5 μm for the nadir angle were 0.997 and 0.984 for the fine dendrite snow, 0.996 and 0.974 for the medium granular snow, 0.995 and 0.971 for the coarse grain snow, 0.992 and 0.968 for the sun crust, and 0.993 and 0.949 for the bare ice, respectively. In addition, the spectral contrast exhibits a strong angular dependence, particularly for the coarser snow and bare ice, e.g., the emissivity at $\lambda = 12.5\ \mu\text{m}$ for the off-nadir angle of 75° reaches down to 0.927, 0.896, and 0.709 for the coarse grain snow, sun crust, and bare ice cases, respectively. The angular dependent emissivity spectra of the bare ice were quite consistent with the spectra predicted by the Fresnel reflectance theory. The observed results firmly demonstrate that the directional emissivity of snow in the TIR can vary depending upon the surface snow type. The high variability of the spectral emissivity of snow also suggests the possibility to discriminate between snow and ice types from space using the brightness temperature difference in the atmospheric window.

© 2005 Elsevier B.V. All rights reserved.

Keywords: Directional emissivity; Surface temperature; Snow grain size; Snow and ice; Remote sensing

1. Introduction

The spectral emissivity of snow and ice in the 8–14 μm thermal infrared (TIR) atmospheric window is a key and fundamental surface property for determining snow surface

temperatures from space (Key & Haeffliger, 1992; Wan, 1999; Warren, 1982) and also detecting clouds over cold snow surfaces in the polar night (Liu et al., 2004; Yamanouchi et al., 1987). The Moderate Resolution Imaging Spectroradiometer (MODIS) land surface temperature retrieval algorithm, for example, needs to determine the appropriate emissivity spectra from pre-determined land-cover types (Snyder et al., 1998; Wan, 1999). The remote sensing of tropospheric trace gases using a nadir-looking

* Corresponding author.

E-mail address: hori@eorc.jaxa.jp (M. Hori).

imaging infrared Fourier-transform spectrometer such as Interferometric Monitor for Greenhouse gases (IMG) onboard Advanced Earth Observing Satellite (ADEOS) and Tropospheric Emission Spectrometer (TES) aboard NASA's AURA satellite also needs a priori emissivity spectrum of the target surface for the accurate retrieval (Beer et al., 2001; Clerbaux et al., 2002). For those applications, there are several spectral emissivity libraries available for various terrestrial surfaces including snow and ice (e.g., ASTER Spectral Library (1999); MODIS University of California, Santa Barbara (UCSB) Emissivity Library (Wan & Zhang, 1999)).

The spectral emissivities of snow in the TIR have been investigated based on the radiative transfer theory and/or the measurements of the directional–hemispherical reflectance (DHR; DHR can be equalized to $1 - \epsilon$ using Kirchhoff's law, where ϵ is the directional emissivity at a given exitance angle.) conducted in a laboratory. Berger (1979) adapted a simple geometric optics approximation to the scattering problem at the large absorption limit and indicated that the emissivity exhibits a weak dependence on the snow density. Dozier and Warren (1982) simulated the DHR of snow based on a more rigorous treatment, i.e., Mie scattering theory for single scattering and delta-Eddington approximation for multiple scattering, and showed that the DHR in the TIR has a significant angular dependence, but little dependence on the snow physical parameters such as grain size and density. Most of the algorithms retrieving snow surface temperatures from space have then been developed based on the results of Dozier and Warren (e.g., Key & Haefliger, 1992; Key et al., 1997; Snyder et al., 1998).

However, a laboratory measurement study revealed that the DHR of snow can vary also depending on the snow type ranging from frost, fine new snow, medium and coarse granular snow to crust even at a near-nadir incidence angle (10°), in other words, snow emissivity in the 8–14 μm atmospheric window decreases with increasing the grain size, which is quite different from the past simulation results (Salisbury et al., 1994). Wan et al. (1999) also obtained similar spectral emissivities at the same incidence angle of 10° for medium granule snow samples in a cold laboratory but without detailed characterization of the snow particle type. Their results suggest that the Mie scattering theory assumed in the Dozier and Warren's studies fails in simulating the light scattering processes in a closely packed and non-spherical particle medium like snow, particularly for coarse and welded snow, in which the independent scattering approximation is considered to be no longer applicable. Wald (1994) then succeeded in modeling the spectral DHR of the disaggregated coarse granular snow and welded snow obtained by Salisbury et al. (1994). The former DHR of the disaggregated snow was modeled by employing the “diffraction subtraction method” in which the diffracted components of the scattered light was subtracted in the radiative transfer simulation for a close-packed snow media, while the latter DHR of the welded snow was expressed as the weighted sum of the radiative transfer reflectance and the Fresnel reflectance. Wald (1994) also pointed out that the angular dependence determined with any radiative transfer theory is only applicable for disaggregated

snow samples, and the emissivity of welded samples should be partly accounted for using the Fresnel reflectance theory which has a strong angular dependence. Therefore, not only grain size but also cementation effects, i.e., welded or disaggregated, can be considered as important factors that determine the directional emissivity of snow.

Nevertheless, the results of the past DHR measurements in the laboratory have been confined to the spectra at a single incidence angle of 10° due to the limitation of the instrument design (e.g., Korb et al., 1999; Salisbury et al., 1994; Wan et al., 1999), and thus the angular dependence have never been verified. Also, in-situ measurements of the directional emissivity have never been made in conjunction with the detailed characterization of the snow in order to validate the current knowledge on snow emissivity. This is because field measurements of the spectral emissivity require (1) employing a robust and portable battery-powered instrument to carry into the desired fields, (2) performing more delicate operations of the instrument and more complex data analysis procedures than in the laboratory due to the variable environmental conditions in the fields such as temperature, winds, solar radiation, etc., and thus (3) carrying out the measurements under cloudless and stable weather conditions, all of which reduce the chances to have good measurements compared with that in the laboratory. However, snow cover in the real fields can experience various metamorphose, sintering, and melting processes even over a short period and thus snow grains can rapidly change their form and size within a day particularly in the melting season. Therefore, it is desirable and important to measure the emissivity of a snow surface as it is in the field without any time lags from the other observations to be compared such as snow pit work, ground based optical measurements, and airborne/satellite observations for validation.

In this study, we derive the spectral directional emissivity of snow and ice surfaces for the first time from the spectral radiances in the 8–14 μm window measured at several viewing angles in the real fields in conjunction with snow pit work using a portable battery-powered Fourier-transform infrared spectroradiometer (FT-IR) (Korb et al., 1996). We then investigate the dependence of the spectral emissivity on the snow type (grain size and shape) and exitance angle, and also validate the past laboratory and simulation results. Our results indicate that the experimental approaches employed in this study can be a pioneer in the measurement of the spectral directional emissivity of various snow types in the real fields complemented by detailed characterization of the snow relating the directional emissivity variations to the variations of the physical conditions of the snow surface and also establishing a procedure to perform in-situ measurements of snow emissivity in a cold environment.

2. Experiments

2.1. Observation sites and periods

Field experiments for measuring the spectral radiances in the TIR were carried out in the daytime at several snow fields

located in eastern Hokkaido, Japan, in February 2002 and March 2004 and also in a snow field in the Alaskan tundra located about 5 km northeast of Barrow in April 2003. The observation dates, place, exact locations, and the type of the sites are summarized in Table 1. The ground surfaces at all the sites are wide and flat without any obstacles for the measurements of the optical properties of snow at the ground. Also, our site in Barrow is located about 2 km south of the North Slope of the Alaska site, one of the Atmospheric Radiation Measurement (ARM, <http://www.arm.gov/sites/nsa/barrow.stm>) Program sites, which is measuring various atmospheric radiation and meteorological conditions.

2.2. Snow characterization

The vertical structure of the snow physical parameters such as snow depth, snow type, and grain size was measured by snow pit work near the optical measurement site except for the case on March 18, 2004, when the site was covered with smooth bare ice without snow cover, and thus, only the ice thickness was measured (see Table 1). For measuring the snow type and grain size, we used handheld loupe with scale and a digital microscope. For this study, the snow physical properties observed in the surface layer within a 0.5 cm depth were used for the comparison with the spectral emissivities of snow in the TIR derived from the FT-IR measurements. This is because the skin depth of the TIR radiation in the snow layer can be considered to be on the order of millimeters due to the large imaginary part of the complex refractive indices of ice throughout the TIR wavelength range (Warren, 1982).

2.3. Thermal infrared radiance measurements

The TIR radiances of the target surfaces were measured with a portable battery-powered FT-IR spectrometer (Model 102FW, Designs and Prototypes, Ltd., USA). It measures the thermal emission at $\lambda=2\text{--}5\ \mu\text{m}$ with a indium antimonide (InSb) detector and the emission at $\lambda=8\text{--}14\ \mu\text{m}$ with a mercury cadmium telluride (HgCdTe) detector at a $4\ \text{cm}^{-1}$ resolution and at a scan rate of 1 scan per second (The effective spectral resolution for measured spectra is actually reduced to around $15\ \text{cm}^{-1}$ due to the apodization process employed. In this study all the spectra measured or simulated are then convolved to have the same spectral resolution before the spectral analysis.). The optical throughput is $0.016\ \text{cm}^2$ steradian and the weight is 6.8 kg. The FT-IR instrument is the winterized package of the standard Model 102F instrument and can be operated at temperatures down to $-20\ ^\circ\text{C}$ in cold environments. Basic specifications of the instrument (fore-optics, interferometer, and detector) are the same as the older model as described by Korb et al. (1996). For the radiance calibration, a blackbody connected to the instrument is controlled to go to temperatures just below or above the sample temperature and then the blackbody radiance is measured by the instrument. The emissivity of the temperature-controlled blackbody and its temperature stability are $0.994\text{--}0.998\pm 0.002$ and $\pm 0.1\ ^\circ\text{C}$, respectively, both of which translate into a combined calibra-

tion error caused by the blackbody of less than a factor of 0.004 (Korb et al., 1996). The temperatures of the interferometer are also maintained constant within $0.1\ ^\circ\text{C}$, which limits the fractional calibration error to less than 0.002 (Korb et al., 1996). For acquiring the one spectrum output, several spectra (typically 10 spectra) are averaged into a coadded spectrum to reduce the noise. Fore-optics can rotate around a horizontal axis to view a target on the ground surface at any viewing angle. In this study, however, the FT-IR instrument is always placed at a fixed position during the measurements, and thus the same target area cannot be structurally observed at different viewing angles.

To obtain the directional emissivity spectra of a sample target we defined a series of FT-IR measurements consisting of the following order: (step 1) measurements of warm blackbody, gold diffuse plate, and cold blackbody, (step 2) measurements of the sample surface at six different viewing angles (0° , 15° , 30° , 45° , 60° , 75°), and finally (step 3) the same measurements as (step 1). A gold diffuse plate ($5\times 5\ \text{in.}$, Labsphere, Inc., USA, IRT-94-050) was used in steps 1 and 3 for measuring the atmospheric downwelling radiances. A series of measurements (steps 1–3) should be completed as fast as possible so as not to be affected by the variation in the instrument self-emission that can vary with the change in the temporal weather conditions in the fields. We performed one series of measurements typically within about 10 min. The raw spectra of the samples were calibrated to the radiance spectra L_{sample} using warm and cold blackbody measurements based on the same procedures as those described by Korb et al. (1996), except that we also took into account temporal drift of the blackbody raw spectra during a series of measurements using two pairs of warm and cold blackbody spectra acquired in (step 1) and (step 3). In addition, the temperatures of the fore-optics, gold diffuse plate, the air, and the snow surface were monitored with thermistors to detect any changes in the thermal environmental conditions that affect the accuracy of the FT-IR measurements.

2.4. Shortwave infrared reflectance measurements

The snow spectral reflectance in the near infrared (NIR) and shortwave infrared (SWIR) regions corresponding to local minima in the absorption coefficient of ice (e.g., $\lambda=0.8\text{--}1.2\ \mu\text{m}$, $1.8\ \mu\text{m}$, and $2.2\ \mu\text{m}$) has a strong dependence on the snow grain size in the surface layer (Wiscombe & Warren, 1980). Then, we measured the snow spectral reflectance at the observation sites to assess the relationship between the snow grain size obtained by the snow pit work and the snow emissivities in the TIR measured with the FT-IR instrument. For this purpose, the reflectances at the wavelengths $\lambda=1.64\ \mu\text{m}$ and $2.2\ \mu\text{m}$ among the NIR and SWIR regions are used in this study because the shallow penetration depth of light within a 1 cm depth at those wavelengths (e.g., Li et al., 2001) is close to the skin depth of the TIR radiation mentioned above as opposed to the cases in the shorter wavelength regions (As the wavelength become shorter, the penetration depth of light becomes deeper, and furthermore, the effect of snow impurity on the snow reflectance becomes nonnegligible.). Those two

Table 1
Summary of the field experiment sites and snow pit-work results during the observation period (2002–2004)

Date/year	Place, Lat./Lon.	Site type	Snow depth	Air/surface temperature	Snow grain shape ^a [graphic symbol ^b] (depth: 0.0–0.5 cm)	Classified surface type [snow grain diameter median, min–max]	Notes
26 Feb/2002	Saroma, Hokkaido (Japan), 44° 7' 9" N/143° 55' 46" E	Snow cover over frozen lagoon	7.5 cm	1~2 °C/–2~0 °C	New snow [+], lightly compacted snow [/], faceted crystals [□]	Fine dendrite snow [70, 40–100 μm] (Photo: Fig. 7a)	The surface is mainly covered with a thin blanket of new snow. The sky is clear.
26 Apr/2003	Barrow, Alaska (USA), 71° 18' 28" N/156° 37' 40" W	Snow cover over tundra	24 cm	–4~0 °C/–8~–3 °C	New snow [+] consisting of broken dendrites and ice pellets	Coarse grain snow [800, 50–1000 μm] (Photo: Fig. 7c)	The surface snow cover is relatively spatially heterogeneous in terms of grain shape. The photo in Fig. 7c corresponds to the case of the ice pellets. The sky is clear.
15 Mar/2004	Abashiri, Hokkaido (Japan), 43° 58' 15" N/144° 11' 37" E	Snow cover over frozen lake	17 cm	–1.5~0 °C/–2~0 °C	Granular snow [○], new snow [+]	Medium granular snow [600, 300–1100 μm] (Photo: Fig. 7b)	The surface is covered with a mixture of granular snow and new snow in this order of fraction. The sky is clear.
18 Mar/2004	Saroma, Hokkaido (Japan), 44° 7' 25" N/143° 58' 7" E	Bare ice area of frozen lagoon	15 cm (as ice)	–3~–2 °C/–3~–2 °C	Smooth bare ice without snow cover	Bare ice [not determinable] (Photo: Fig. 7e)	The surface is covered with a smooth dark ice which is refrozen melted-snow partly mixed with seawater with a low roughness on the order of millimeters in height. Strong winds blow over the site. The sky is clear around the zenith, but there are some low-level clouds near the horizon.
24 Mar/2004	Nakashibetsu, Hokkaido (Japan), 43° 29' 56" N/144° 42' 50" E	Snow cover over grassland	91 cm	1~2 °C/–1~0 °C	Sun crust [–], granular snow [○]	Sun crust [1100, 800–1500 μm] (Photo: Fig. 7d)	The surface is mainly covered with a thin welded sun crust. Grain size shown left is the dimension of each grain aggregating into a crust. One piece of a crust can be larger than 5 mm. The sky is almost clear but partly covered with thin cirrus clouds.

^a The definitions of snow grain shape are principally based on those defined by Japanese Society of Snow and Ice (1998).

^b Graphic symbols are based on the international classification of snow crystals if available (Colbeck et al., 1990).

wavelengths are located in the transparent regions of the atmospheric transmittance (one of the local minima in the absorption coefficient of ice at $\lambda = 1.8 \mu\text{m}$ could be affected by the strong water vapor absorption) and thus are commonly selected to the center wavelengths of the spectral bands for the spaceborne spectral radiometers (e.g., the Enhanced Thematic Mapper Plus (ETM+) onboard LAND remote sensing Satellite-7 (Landsat-7) and Global Imager (GLI) onboard Advanced Earth Observing Satellite-II (ADEOS-II)). The spectral reflectance (flux reflectance defined by the ratio of the upward reflected flux to the downward incident solar flux) of snow in the SWIR was measured using a grating-type spectrometer, FieldSpecFR (ASD, Inc., USA). We used the observation system which employs a white reference standard made by Labsphere, Inc. (USA) to measure the downward and upward radiant flux for the reflectance calculation. Detailed methods of the reflectance observations are the same as those described by Aoki et al. (2000).

2.5. Monitoring of the sky condition

To select the appropriate TIR radiance samples for the emissivity derivation, we monitored the change in the sky weather and atmospheric conditions using a sky-viewing digital camera (Nikon, Coolpix995) with a fish-eye converter lens (FC-E8) and net-radiometer (Kipp and Zonen, CNR-1) at the site. Only at the Barrow site were additional data such as atmospheric downwelling radiance spectra measured by the Atmospheric Emitted Radiance Interferometer (AERI) (Demirgian & Dedecker, 2005) and micropulse lidar measurements, etc., provided by the ARM program (data were obtained from the ARM data archive; <http://www.archive.arm.gov/cgi-bin/arm-archive>, accessed on July 17, 2003) also taken into account. By examining these sky condition datasets, as far as possible, we eliminated the poor data of the FT-IR measurements acquired under highly variable and/or cloudy weather conditions from the spectral analysis for the emissivity derivation described below in Sections 3.1–3.3.

3. Emissivity derivation

In general, the directional emissivity of a target sample is derived from the sample radiance (L_{sample}) by the following equation (Korb et al., 1999),

$$\varepsilon_{\text{sample}}(\lambda, \theta_{\text{ext}}) = \frac{L_{\text{sample}}(\lambda, \theta_{\text{ext}}) - L_{\text{dwr}}(\lambda, \theta_{\text{eff}})}{B(\lambda, T_{\text{sample}}) - L_{\text{dwr}}(\lambda, \theta_{\text{eff}})}, \quad (1)$$

where $\varepsilon_{\text{sample}}(\lambda, \theta_{\text{ext}})$ is the directional emissivity at the wavelength λ for the exitance (viewing) angle θ_{ext} , T_{sample} is the true physical temperature of the sample surface, $B(\lambda, T_{\text{sample}})$ is the isotropic Planck radiance at the wavelength of λ and the temperature of T_{sample} , and $L_{\text{dwr}}(\lambda, \theta_{\text{eff}})$ is the effective downward emission from the atmosphere at an effective incidence angle of θ_{eff} to be reflected into the spectrometer.

As inferred from Eq. (1), in addition to L_{sample} measured by FT-IR, both $L_{\text{dwr}}(\lambda, \theta_{\text{eff}})$ and T_{sample} are the key parameters to

be determined for the derivation of the directional emissivity spectra. In this study, we used the atmospheric downwelling radiances simulated using a radiative transfer code as the former key parameter $L_{\text{dwr}}(\lambda, \theta_{\text{eff}})$ in Eq. (1) instead of employing the downwelling radiances measured with the gold diffuse plate in order to take into account the anisotropy of the downwelling radiance. For the determination of the latter key parameter T_{sample} , we used the measured sample radiance and also both the measured and simulated downwelling radiances by making use of a spectral contrast of the atmospheric downwelling radiance at around the edge of the atmospheric window where the emissivities of snow and ice surfaces are expected to be constant. The details of those methods are described below in this Section 3.

3.1. Selection of the downwelling radiance

In the field experiment studies, the atmospheric downwelling radiance L_{dwr} is generally observed in the reflection from the diffusely reflective gold or brass plates located near the samples (Korb et al., 1996, 1999), which is given by the following equation,

$$L_{\text{dwr}}(\lambda) = \frac{L_{\text{sample,gdp}}(\lambda) - \varepsilon_{\text{G}}(\lambda)B(\lambda, T_{\text{G}})}{1 - \varepsilon_{\text{G}}(\lambda)}, \quad (2)$$

where ε_{G} is the emissivity of the gold diffuse plate (ε_{G} of 0.1 is adopted from ASTER Spectral Library (1999) in this study), $B(\lambda, T_{\text{G}})$ is the isotropic Planck radiance at the wavelength of λ and the temperature of T_{G} , $L_{\text{sample,gdp}}(\lambda)$ is the measured radiance looking at the gold diffuse plate and thus includes both the reflected downwelling radiance and the thermal emission from the gold diffuse plate itself. This method gives no directional dependent downwelling radiance, but rather provides a single downwelling radiance at an effective incidence angle of around 45° representing the average of the downward emission from the atmosphere in the hemispherical field of view of the sample (Hereafter, L_{dwr} on the left-hand side in Eq. (2) derived from the FT-IR measurements of the gold diffuse plate is referred to as L_{GDP}).

However, the angular dependence of L_{dwr} could be an important factor in the derivation of the absolute emissivity when the surface reflection property is not diffuse (Lambertian) but rather close to the specular type with a high reflectance to be expected for such welded snow and smooth bare ice. Fig. 1 shows an example of the calibrated sample radiances (L_{sample}) in the TIR measured at the six viewing angles on a smooth bare ice surface on March 18, 2004. Also shown are the spectra of the warm and cold blackbody radiances used for the calibration. As expected from the Fresnel reflectance theory (Wald, 1994), the calibrated radiances of bare ice exhibit a strong angular dependence. In addition, it is apparent that as the viewing angle increases, the contribution of the reflected atmospheric downwelling radiances to L_{sample} becomes significant, which is indicated by the small peaks in L_{sample} at the major atmospheric absorption bands (e.g., O_3 : $\lambda = 9.4\text{--}10.0 \mu\text{m}$, H_2O : $11.7 \mu\text{m}$

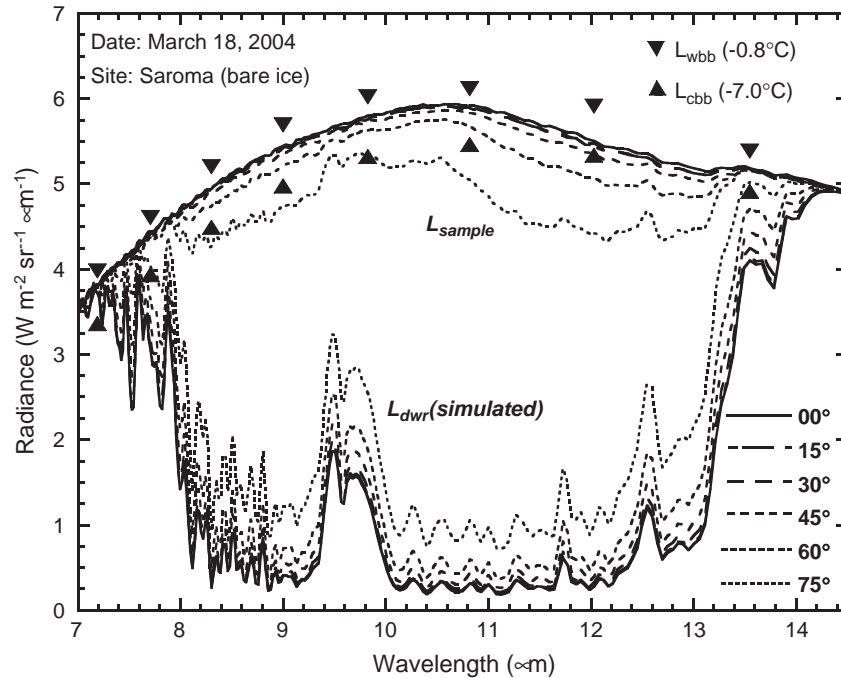


Fig. 1. Spectra of calibrated radiances from smooth bare ice measured at six viewing angles by FT-IR. Spectra of warm and cold blackbody radiance used for calibration are shown by downward and upward solid triangle symbols, respectively. Also shown are the spectra of the atmospheric downwelling radiances at six incidence angles simulated using MODTRAN4 with JMAOA atmospheric profile data.

and 12.6 μm). This can be considered not simply because the emissivity of the ice surface becomes lower at larger viewing angles, but also due to the anisotropic nature of the downwelling radiances themselves. In Fig. 1 L_{dwr} for six incidence angles are shown as examples which are simulated using the MODTRAN4 radiative transfer code (Berk et al., 1998) along with the Japan Meteorological Agency Objective Analysis (JMAOA) atmospheric profile data which cover $1.25^\circ \times 1.25^\circ$ global grid cells with output every 6 h provided by the Japan Meteorological Agency. Although L_{dwr} at small incidence angles up to 30° does not change much, the angular dependence of L_{dwr} becomes pronounced at the larger incidence angles over 45° . Thus, this angular dependent L_{dwr} should be taken into account for the derivation of the absolute emissivity for such specular surfaces. In this study, therefore, for the correction of the downwelling radiance component in L_{sample} we chose to simulate the angular dependent downwelling radiance ($L_{\text{sim}}(\theta_{\text{inc}})$, θ_{inc} is the incidence angle from vertical) for all sample cases using MODTRAN4 along with the JMAOA data as shown in Fig. 1 instead of using L_{GDP} .

There are also other reasons for employing L_{sim} instead of L_{GDP} for the downwelling radiance correction. Because the response of the FT-IR system with the HgCdTe detector to very cold targets, such as the clear dry skies, is highly nonlinear at wavelengths around 11.8 μm in the 8–14 μm window (Korb et al., 1996), the measured atmospheric downwelling radiance can contain a significant calibration artifact. Fig. 2 shows the comparison of L_{GDP} with $L_{\text{sim}}(0^\circ)$, $L_{\text{sim}}(45^\circ)$, and $L_{\text{sim}}(75^\circ)$ for the case at Barrow on April 26, 2003. Inside the atmospheric window around $\lambda=8\text{--}13.2\ \mu\text{m}$, L_{GDP} was found to be too high compared with L_{sim} due to the spectral artifacts caused by the

nonlinear response of the FT-IR system, whereas outside of the window, L_{GDP} is very consistent with $L_{\text{sim}}(45^\circ)$ (see the curve “ $L_{\text{sim}}(45^\circ)$ vs. L_{GDP} ” in the lower part of Fig. 2). It should be noted here that because the atmospheric downwelling radiance is no longer anisotropic at the wavelengths $\lambda=14.2\text{--}14.4\ \mu\text{m}$ outside the atmospheric window as shown in Figs. 1 and 2, L_{GDP} is applicable for L_{dwr} in Eq. (1) only at those wavelengths.

Also shown in Fig. 2 is the AERI measured downwelling radiance from the zenith (L_{AERI}) acquired at the same observation time as the FT-IR measurement. AERI has been developed to measure the atmospheric downwelling radiance at the surface with a high absolute radiometric calibration of better than 1% (Knuteson et al., 2004a,b). L_{AERI} is found to be the most consistent with $L_{\text{sim}}(0^\circ)$. The difference between $L_{\text{sim}}(0^\circ)$ and L_{AERI} is mostly less than 10% (average: -2% , standard deviation: 5%) in the measured wavelength region and becomes a maximum of about 14% at the wavelengths where the maximum error of $L_{\text{sim}}(0^\circ)$ is evaluated (see the curve “ $L_{\text{sim}}(0^\circ)$ vs. L_{AERI} ” in Fig. 2). This indicates that the MODTRAN calculation succeeds in simulating the actual downwelling radiance within the errors of 14%.

3.2. Determination of the surface temperature

The second key parameter T_{sample} , to be determined for the derivation of the spectral directional emissivity spectra, is not the temperature of bulk snow or ice, but that of the skin layer of the surface being typically of the order of millimeters in depth from which snow or ice emits infrared radiation upward. It is difficult to directly measure T_{sample} with a temperature probe such as a thermistor in the field because solar radiation heats

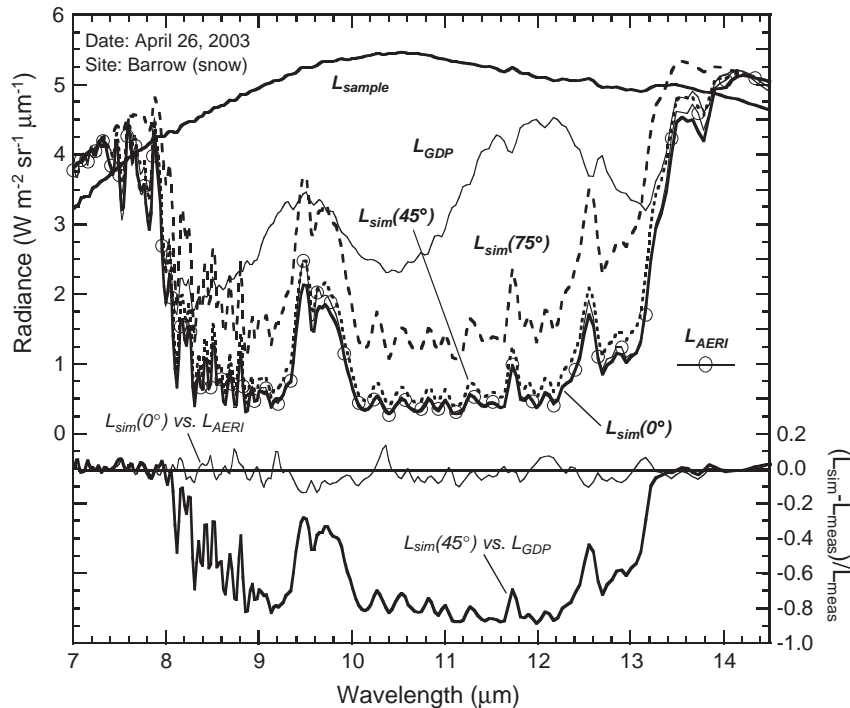


Fig. 2. Comparison of the downwelling radiance spectra obtained by various methods; L_{sim} : MODTRAN4 simulation at the incidence angles (θ_{inc}) of 0° (thick solid line), 45° (dotted line), and 75° (dashed line), L_{GDP} : FT-IR measurement with the gold diffuse plate (solid line), and L_{AERI} : AERI measurement (thin solid line with open circle). L_{sample} is a snow radiance spectrum (thick solid line). Also, the curves in the lower part of the figure are the differences between the simulated and measured downwelling radiance spectra ($L_{sim}(0^\circ)$ vs. L_{AERI} (thin solid line) and $L_{sim}(45^\circ)$ vs. L_{GDP} (thick solid line)) shown as a fraction of the latter measured spectra in the right axis (L_{meas} denotes L_{AERI} or L_{GDP}).

the probe and thus causes an error of the measured temperature. We then determined T_{sample} for individual FT-IR spectra by solving simultaneous equations set up with Eq. (1) for the pairs of L_{sample} and L_{dwr} at two wavelengths closely located inside ($\lambda = 13.0 \mu\text{m}$) and outside ($\lambda = 14.2 \mu\text{m}$) the atmospheric window at which the spectral emissivities are expected to be nearly constant. Fig. 3 summarizes the analysis procedure to derive T_{sample} and emissivity from the measured and simulated radiance spectra. The nearly isotropic L_{dwr} outside the atmospheric window is derived from the FT-IR measurements of the gold diffuse plate (L_{GDP}) by Eq. (2), whereas the anisotropic L_{dwr} inside the window is determined from among the radiances simulated for six incidence angles by MODTRAN (L_{sim}).

Past laboratory experiments revealed that the emissivities of snow and ice at around $\lambda = 13.0\text{--}14.2 \mu\text{m}$ at $\theta_{ext} = 10^\circ$ were nearly constant within 0.005 as shown in Fig. 4 (Salisbury et al., 1994; Wan & Zhang, 1999). Although the directional snow emissivity at larger exitance angle cases has never been well characterized by measurements, the Fresnel reflectance theory predicts that variations in the ice emissivity at $\lambda = 13.0\text{--}14.2 \mu\text{m}$ are less than 0.015 even at $\theta_{ext} = 75^\circ$ (emissivity is around 0.7; not shown in the figures). Therefore, we assume that the emissivities of snow and ice at $\lambda = 13.0$ and $14.2 \mu\text{m}$ are the same with the possible emissivity differences within 0.005 (for $\varepsilon = 0.9\text{--}0.015$ ($\varepsilon = 0.7$)).

As shown in Fig. 1, L_{dwr} inside the atmospheric window is significantly smaller than the snow radiances and is furthermore anisotropic, whereas L_{dwr} becomes comparable to the snow

radiance and is isotropic outside the window ($\lambda = 14.2\text{--}14.4 \mu\text{m}$) due to the opacity of the atmosphere (the strong downward emission from the lower atmosphere). The strong contrast of L_{dwr} at around the wavelength edge of the atmospheric window results in different sensitivities of T_{sample} to ε_{sample} in Eq. (1) on both sides of the window edge. Fig. 5 shows an example of the relationship between T_{sample} and ε_{sample} derived from the radiances at both $\lambda = 13.0 \mu\text{m}$ and $14.2 \mu\text{m}$ (thick solid curves) measured at Barrow on April 26, 2003. Also shown are the possible relations of T_{sample} with ε_{sample} simulated for different $BT_{GDP} - BT_{sample}$ cases at $\lambda = 14.2 \mu\text{m}$ (BT_{GDP} and BT_{sample} are the brightness temperatures derived from the measured radiances L_{GDP} and L_{sample} , respectively, using the Planck function) and different incidence angle cases of L_{sim} at $\lambda = 13.0 \mu\text{m}$ (both shown in thin dashed lines). The dependence of T_{sample} on ε_{sample} is weak outside the window ($\lambda = 14.2 \mu\text{m}$), while T_{sample} moderately depends on ε_{sample} inside the window ($\lambda = 13.0 \mu\text{m}$). As a result, when L_{sample} is exactly the same as L_{GDP} at $\lambda = 14.2 \mu\text{m}$, the physical temperature T_{sample} can be directly determined as the brightness temperature of L_{sample} independently of the surface emissivity, which corresponds to the horizontal broken line ($BT_{GDP} - BT_{sample} = 0 \text{ K}$) in the figure. Even for the case when L_{sample} is not consistent with L_{GDP} ($BT_{GDP} \neq BT_{sample}$) as the example of April 26, 2003, shown in Fig. 5, under the constant emissivity assumption, T_{sample} can be determined as the crossing point of the curves of T_{sample} derived for $\lambda = 13.0 \mu\text{m}$ and $14.2 \mu\text{m}$.

Here, we estimate the possible fractional errors in the derived emissivity resulted from the T_{sample} determination

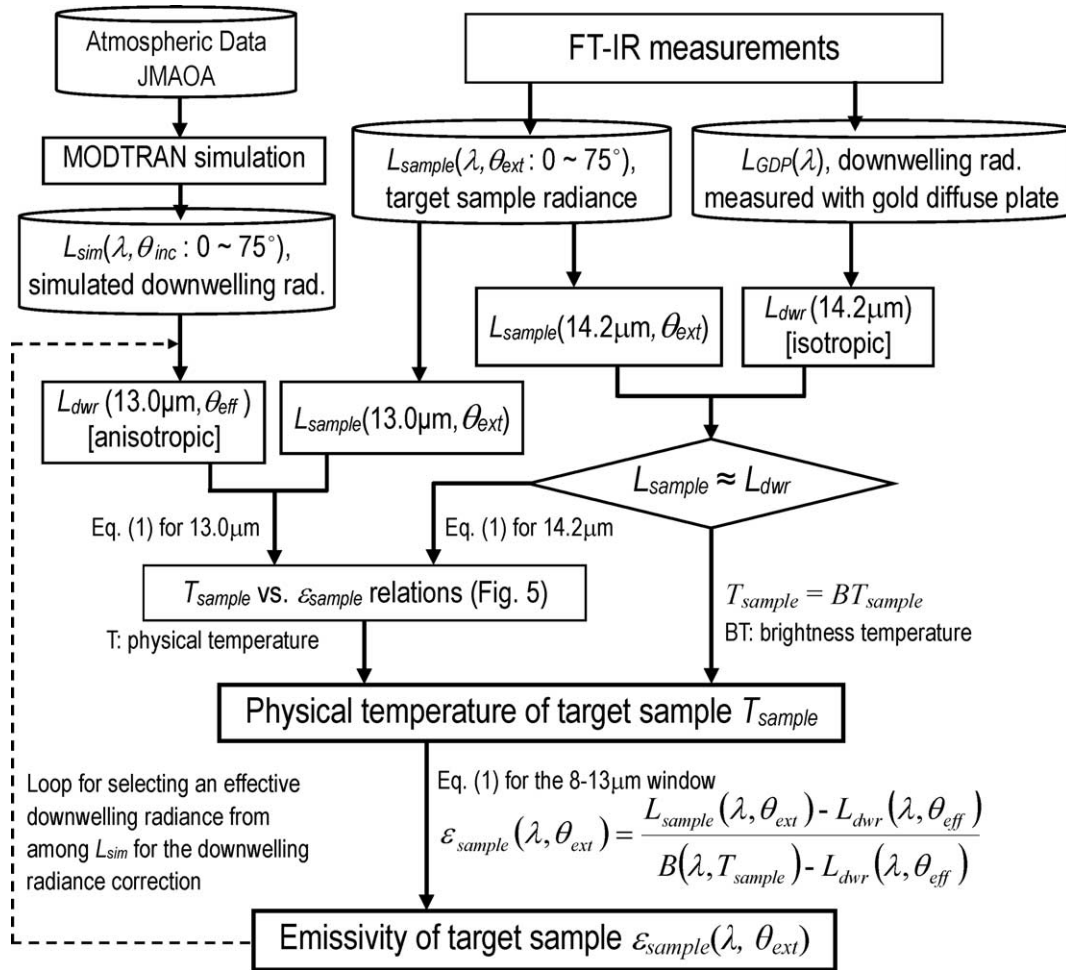


Fig. 3. Flowchart of the FT-IR spectra analysis used to derive physical temperatures (T_{sample}) and emissivities (ϵ_{sample}) of the sample surfaces for the six exitance angle cases of $\theta_{ext}=0, 15, 30, 45, 60, 75^\circ$. An effective downwelling radiance $L_{dwr}(\lambda, \theta_{eff})$ is selected from among the simulated downwelling radiances (L_{sim}) at incidence angles θ_{inc} from 0 to 75° so as to provide the smoothest emissivity spectrum at the wavelengths of the atmospheric absorption bands (see text in Section 3.3 for details).

process mentioned above. Due to the weak dependence of T_{sample} on ϵ_{sample} at $\lambda=14.2 \mu\text{m}$, the constant emissivity assumption with the possible uncertainty of about 0.005–0.015 at $\lambda=13.0$ – $14.2 \mu\text{m}$ is estimated to cause T_{sample} errors of less than 0.06 K in this study which corresponds to negligible fractional errors of less than 0.001 in the derived emissivity spectra. The heterogeneity of the gold diffuse plate reflectance could also be a source of errors. According to the *ASTER Spectral Library* (1999), the reflectance $r_G (=1 - \epsilon_G, \epsilon_G$ is defined in Eq. (2)) of a Labsphere gold diffuse plate varies depending on the position on the plate with the average reflectance and uncertainty of $r_G=90 \pm 2\%$ at $\lambda=14.2 \mu\text{m}$. This variability in reflectance could cause a fractional error at most in every L_{GDP} measurement of less than a factor of 0.5% which can be translated into the maximum fractional error of less than 0.002 in the derived emissivity spectra.

3.3. Downwelling radiance correction

Once T_{sample} for the individual spectra is determined from the $T_{sample} - \epsilon_{sample}$ relations, then the ϵ_{sample} spectrum is

calculated using Eq. (1). In this process, an effective downwelling radiance $L_{dwr}(\lambda, \theta_{eff})$ is determined in an iterative process shown by the dashed line in Fig. 3 by selecting the most appropriate spectrum from among the downwelling radiances simulated for six incidence angles from 0° to 75° with an interval of 15° ($L_{sim}(0-75^\circ)$). The decision criterion for the radiance selection depends on how much the false peaks seen in the apparent emissivity spectrum around $\lambda=11.7 \mu\text{m}$ and $12.5 \mu\text{m}$ due to the major atmospheric absorption bands can be reduced to provide a smooth absolute emissivity (ϵ_{sample}) spectrum. If necessary, $L_{dwr}(\lambda, \theta_{eff})$ is determined by the interpolation of L_{sim} at two adjacent incidence angles.

As an example, the effect of the downwelling radiance correction on the ϵ_{sample} spectrum is shown for the bare ice case observed on March 18, 2004, in Fig. 6. The upper plot shows the spectra of the apparent emissivity ($=L_{sample}(\lambda, \theta_{ext})/B(\lambda, T_{sample})$) and the lower one shows those of the absolute emissivity (ϵ_{sample}) corrected for the reflected downwelling radiance component. In the upper plot, apparent false peaks in the emissivity spectra due to the atmospheric absorption bands existed. After the correction of the downwelling radiance,

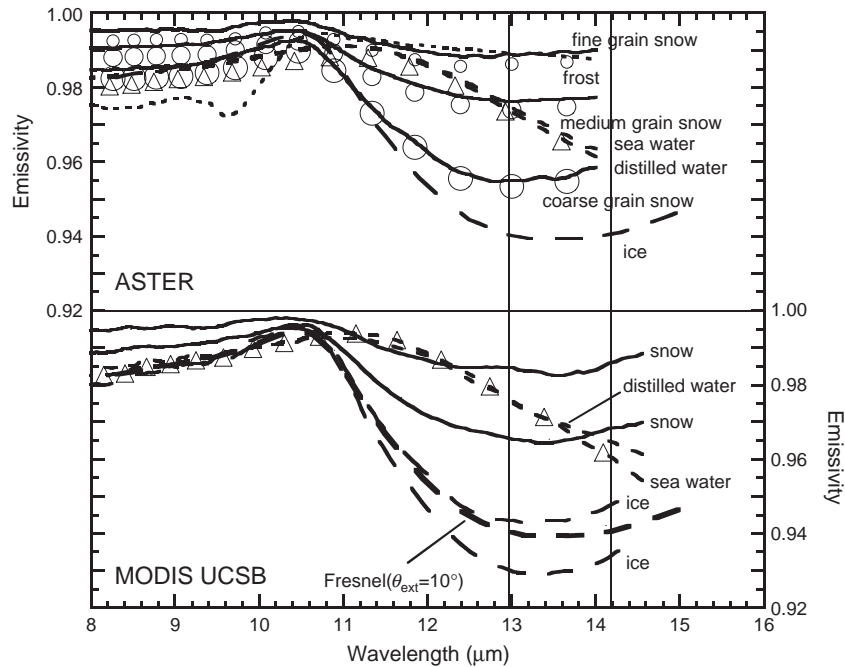


Fig. 4. Typical emissivity spectra of snow, ice, distilled water, and sea water in TIR obtained at the exitance angle $\theta_{ext}=10^\circ$ by past laboratory experiments reproduced from the *ASTER Spectral Library* (1999) and from the MODIS University of California, Santa Barbara (USCB) Emissivity Library (Wan and Zhang, 1999). Also plotted are the spectra of ice derived from the Fresnel reflectance theory for the same exitance angle.

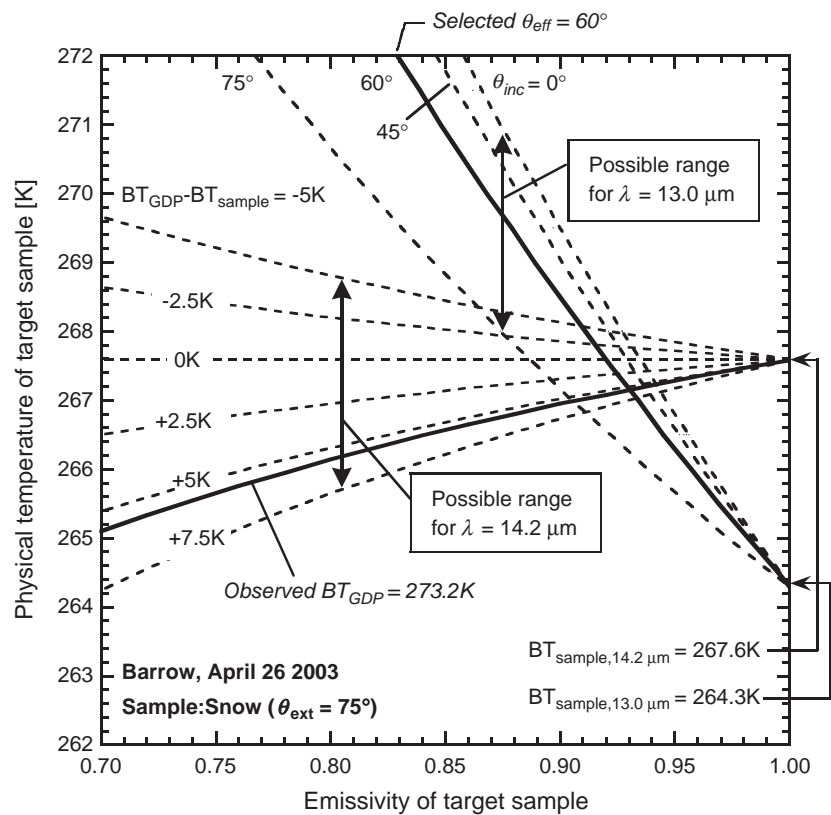


Fig. 5. Relations between physical temperature (T_{sample}) and emissivity (ϵ_{sample}) for the snow surface at Barrow on April 26, 2003, derived using Eq. (1) with radiances at two wavelengths inside ($\lambda=13.0\ \mu\text{m}$) and outside ($\lambda=14.2\ \mu\text{m}$) the atmospheric window. Thick solid lines indicate actual determined relations in the FT-IR spectra analysis (Fig. 3) derived from the selected L_{sim} for $\lambda=13.0\ \mu\text{m}$ and the observed L_{GDP} for $\lambda=14.2\ \mu\text{m}$. Thin dashed lines show possible $T_{sample} - \epsilon_{sample}$ relations for various L_{sim} and L_{GDP} conditions.

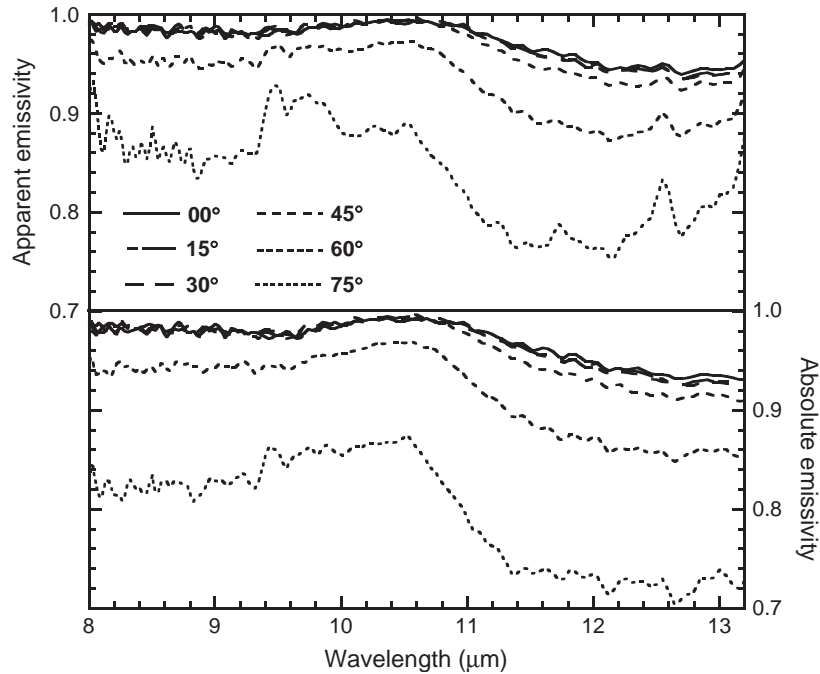


Fig. 6. An example of the directional emissivity spectra before (apparent emissivity, upper plots in the figure) and after (absolute emissivity, lower plots) the downwelling radiance correction shown for the six exitance angles of $\theta_{\text{ext}}=0^\circ, 15^\circ, 30^\circ, 45^\circ, 60^\circ, 75^\circ$. Sample target is bare ice observed on March 18, 2004.

however, the apparent peaks are clearly reduced and become a portion of a smooth curve in the individual spectra as shown in the absolute emissivity spectra.

4. Results and discussion

4.1. Snow and ice surface and the sky conditions

Results of the snow pit work measurements during the observation periods are summarized in Table 1. All the experiments were conducted in snow covers at least 7.5 cm in depth which is sufficient for the measurements of TIR radiances except for the case on March 18, 2004, when TIR radiances from the smooth bare ice were measured on a frozen lagoon. The observed snow crystal types are shown in the 6th column as “Snow grain shape”. The definitions of the snow grain shape are based on those defined by the Japanese Society of Snow and Ice (1998) which are similar to the international classification of snow crystals (Colbeck et al., 1990). In Table 1, graphic symbols for each grain shape are also indicated if available based on the latter international classification. Several types of snow crystals were usually found to coexist in the same surface layer. We then classified the snow cover on each day into five different surface types by taking into account the dominant components among the identified grain shapes and also the median diameter of the snow particles, which are shown in the 7th column as “Classified surface type” together with the measured grain diameters. For the crystals with a complex shape such as the dendrite or acicular crystal, the width of the narrower portion, e.g., the branch width, is recorded as the grain size in this study. For the sun crust (also called “firnspiegel”, a thin, glittering ice layer which forms on the surface of a snowpack on sunny days (Ozeki & Akitaya,

1996)), the dimension of each grain aggregating in the crust is recorded.

The classified surface type (fine dendrite snow, medium granular snow, coarse grain snow, sun crust, and bare ice) shown in Table 1 covers various morphological conditions of the snow and ice surfaces possible to appear on the earth ranging from freshly deposited precipitation particles, disaggregated coarse grain snow, and welded snow, to smooth bare ice which is an extreme, ideal example of a flat ice surface. Fig. 7 shows the microphotographs of snow particles collected for the individual classified surface types (note that the order of listing surface types in Table 1 are sorted by observation date, whereas the photographs in Fig. 7 are sorted by grain size). Only for the bare ice case, observed on March 18, 2004 (Fig. 7e), the photograph of the measurement site is shown indicating that the surface is very smooth specular ice with a low roughness on the order of millimeters in height in places. It should be noted, therefore, that although the surface condition of bare ice encountered in this study may be quite different from those mostly found in the thick sea-ice regions, the measurement at the ice surface can provide a valuable opportunity to compare the directional emissivity of the specular ice surface with the theoretical Fresnel reflectance for validation. The sun crust (Fig. 7d) is a thin ice film with a rough surface in contrast to bare ice, which also enables one to verify the validity of the rough surface reflectance model for such a welded block proposed by Wald (1994). Among all the surface types, the snow cover on April 26, 2003 (Fig. 7c), was comparatively spatially heterogeneous in terms of snow grain shape. The surface was covered with a layer of newly fallen precipitation particles but consisting of two distinctly different crystals, i.e., broken dendrites and coarse ice pellets particles

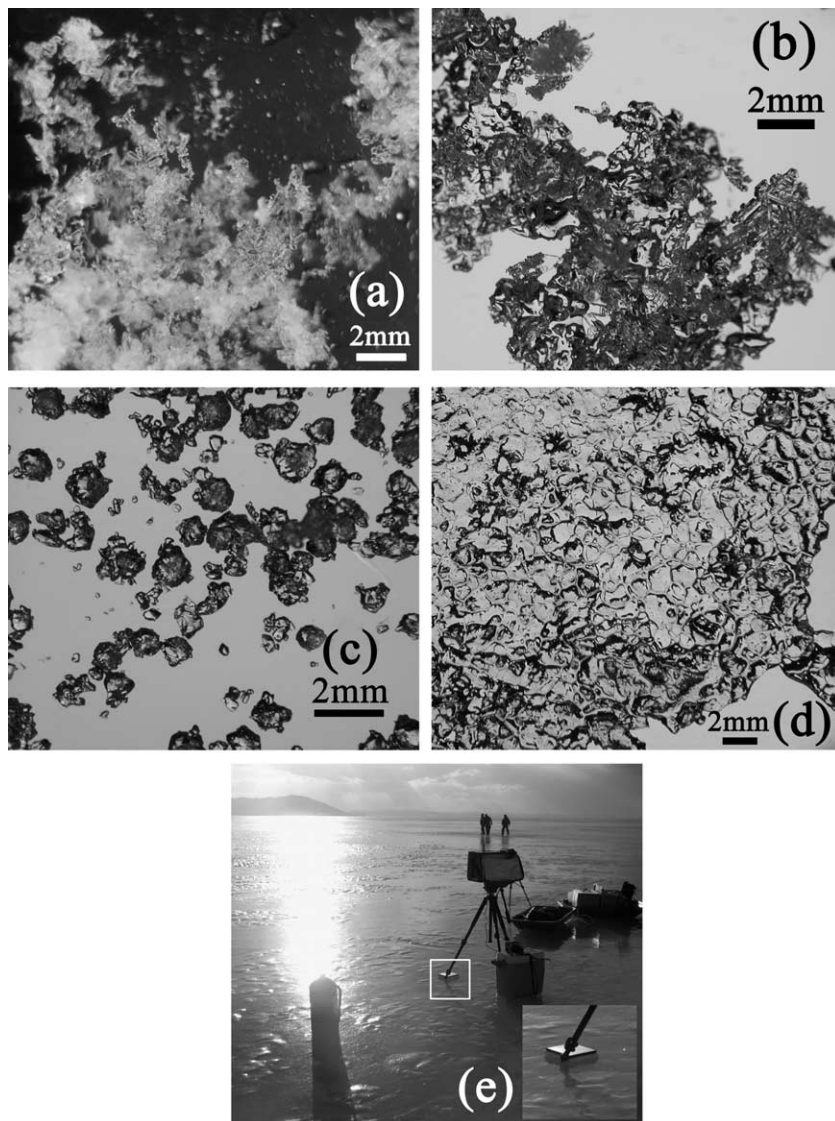


Fig. 7. Microphotographs of snow crystals collected from the surface classified into (a) fine dendrite snow (observed on February 26, 2002), (b) medium granular snow (March 15, 2004), (c) coarse grain snow (April 26, 2003), (d) sun crust (March 24, 2004), and (e) bare ice (March 18, 2004). Only for bare ice the photograph of the measurement site is shown.

depending on the location. Fig. 7c is a photograph of the latter ice pellet case. Additional explanations for the surface and the sky conditions are described for the individual surface types in the notes of Table 1.

The sky conditions were always clear except for the cases on March 18 and 24, 2004. On March 18, the sky was clear around the zenith, but there were some low-level clouds around the part of the sky near the horizon with the cloud fraction of less than 0.1. The multi-angle FT-IR measurements were then performed by pointing the field of view (FOV) of the FT-IR fore-optics to the direction of the clear sky. Considering the specular property of the surface on this day, the effects of the partial clouds on the emissivity results are expected to be negligible. On March 24, the sky was partly covered with thin cirrus clouds which were very thin and thus their effects on the flux reflectance in the SWIR and also on the TIR emissivity observed in this study are considered to be negligibly small.

4.2. Sources of error in the derived emissivities

Several fractional errors have already been estimated in previous sections which are related to the instrument calibration performances (Section 2.3) and the uncertainty of the surface temperature determination (Section 3.2). In this section, we first consider the remaining sources of errors, and then evaluate the possible accumulated errors in the derived emissivity.

4.2.1. Path-radiance contribution to sample radiance

The path length from the sample surface to the instrument fore-optics increases with increasing the viewing angle from about 1 m at the nadir angle ($\theta_{\text{ext}}=0^\circ$) to about 3.9 m at $\theta_{\text{ext}}=75^\circ$. When the surface air is warmer or cooler than the surface, the measured sample radiance at wavelengths outside the atmospheric window (e.g., $\lambda=14.2\ \mu\text{m}$) may differ from the actual radiance emitted from the surface due to the atmospheric

emission and absorption along the optical path from the surface to the detector, which then affects the estimation of T_{sample} (the path radiance effect on L_{sample} is negligible inside the 8–14 μm window in this study due to the low temperature and humidity conditions). In this study, the path radiance effects on L_{sample} are estimated by the MODTRAN4 code under the same viewing angle and temperature conditions as the FT-IR measurements and corrected in the FT-IR spectra analysis. If no corrections were made, possible errors in the emissivity would be 0.002 (at $\theta_{\text{ext}}=0^\circ$)–0.005 (75°) on February 26, 2002, 0.0005–0.002 on March 15, 2004, 0.002–0.009 on April 26, 2003, 0.001–0.003 on March 24, 2004, and 0.0005–0.002 on March 18, 2004.

4.2.2. Temporal variation of the instrument self-emission

Possible emissivity errors due to the fluctuation of the complex instrument self-emission are estimated from the temporal drift of the blackbody radiance spectra measured at the same temperatures during the operation. Estimated errors in the emissivity are plotted in Fig. 8a–e as the absolute values (ERR_{self}, dashed line, right vertical axis) shown together with the derived directional emissivity spectra (OBS00–OBS75, left axis). Also shown are the fractional errors due to the uncertainty of L_{sim} (ERR00–ERR75, solid lines, right axis) which will be discussed in the next subsection.

The values of ERR_{self} are less than 0.005 in most cases, but sometimes exceed 0.005 in some wavelength regions for three cases (February 26, 2002, April 26, 2003, and March 24, 2004) when the instrument temperatures were variable. ERR_{self} on March 18, 2004, is the smallest when the instrument temperature was always kept constant due to the strong winds blowing over the site.

4.2.3. Uncertainty of the simulated downwelling radiance

The maximum error of $L_{\text{sim}}(0^\circ)$ was estimated to be 14% in Section 3.1 based on the comparative results between L_{AERI} and $L_{\text{sim}}(0^\circ)$. We estimated the possible impacts of the uncertainty of L_{sim} upon the determination of the directional emissivity assuming that L_{sim} could vary at the same fraction of $\pm 14\%$ over the entire spectrum. The estimated errors in the emissivity are shown for each exitance angle case (ERR00–75) in Fig. 8 which are the averages of the absolute errors that occurred in the positive (+14%) and negative (–14%) bias cases.

In the case of snow (Fig. 8a–d), the estimated errors are negligible in most of the wavelength regions except for several absorption bands where errors could reach at most 0.003. In the bare ice case (Fig. 8e), errors tend to be larger than those in the snow cases, but become pronounced only at absorption bands at large exitance angle cases being over 0.005 (ERR60) and up to 0.014 (ERR75). These results are due to the derivation of the emissivity as Eq. (1) becomes more sensitive to the bias of L_{dwr} as the emissivity decreases and also as the gap between L_{sample} and L_{dwr} becomes smaller.

4.2.4. Heterogeneity of the surface snow type and roughness

The heterogeneity of the surface in terms of the snow type or roughness can be a source of error for evaluating the

directional emissivity of snow. As the viewing angle increases, the area of the FOV of the FT-IR fore-optics on the surface increases from about 50 cm^2 at $\theta_{\text{ext}}=0^\circ$ to 2900 cm^2 at $\theta_{\text{ext}}=75^\circ$. Thus, for a large viewing angle case, radiances from the surfaces with different snow types or roughness may contribute to the measured radiance spectrum. This could cause an incorrect snow type characterizing the observed directional emissivity or erroneous effective exitance angle. Possible effects of the heterogeneity on the derived emissivity spectra are discussed for individual snow type cases in Section 4.3.2.

4.2.5. Accumulated errors

All of the errors considered above are accumulated to be on the order of 0.01 at most in the wavelength regions except for the atmospheric absorption bands or in the wavelength regions affected by the nonlinearity of the system response at which the errors could exceed 0.01 and may reach 0.02. The estimated accumulated errors are not necessarily small compared with the variation in the snow emissivity spectra with the change in the viewing angle as will be shown in the next section. However, most of the non-negligible errors except for the errors in the absorption bands due to the uncertainty of L_{sim} randomly occur in the positive and negative sign with time. In the derivation of the emissivity spectra shown in Fig. 8, then, the spectra obtained by several series (2–3) of FT-IR measurements were averaged to reduce those random errors. As will be shown later, the consistency of the directional emissivity spectra derived for the smooth bare ice with the spectra predicted from the Fresnel reflectance theory indicates that our approach to derive the absolute emissivity employed in this study is accurate enough to be able to discuss the emissivity differences less than 0.01. Thus, the directional emissivity shown in Fig. 8 can be considered to indicate the actual characteristic of the snow and ice emissivity.

4.3. Characteristics of snow and ice emissivity

4.3.1. Spectral features

The derived emissivity spectra for the five different snow/ice surfaces shown in Fig. 8a–e exhibit two distinct spectral features: 1) an emissivity peak at $\lambda=10.5 \mu\text{m}$ corresponding with a minimum in the single scattering albedo (Mie) of ice in the 8–13 μm window, and 2) a broad emissivity trough (reflectance peak) due to the “reststrahlen band” centered at $\lambda=12–13 \mu\text{m}$ which occurs at the surface-scattering maxima typically associated with the fundamental molecular vibration bands (Salisbury et al., 1994; Wald, 1994). The spectral contrast seen between $\lambda=10.5 \mu\text{m}$ and 12.5 μm is enhanced as snow particles become coarser and welded into a flat crust. For example, the emissivities at $\lambda=10.5 \mu\text{m}$ and 12.5 μm for $\theta_{\text{ext}}=0^\circ$ are 0.997 and 0.984 for fine dendrite snow, 0.996 and 0.974 for medium granular snow, 0.995 and 0.971 for coarse grain snow, 0.992 and 0.968 for sun crust, and 0.993 and 0.949 for bare ice, respectively.

The dependence of the TIR emissivity on the snow grain size observed in this study is quite consistent with the results of the laboratory measurements by Salisbury et al. (1994). Fig. 9

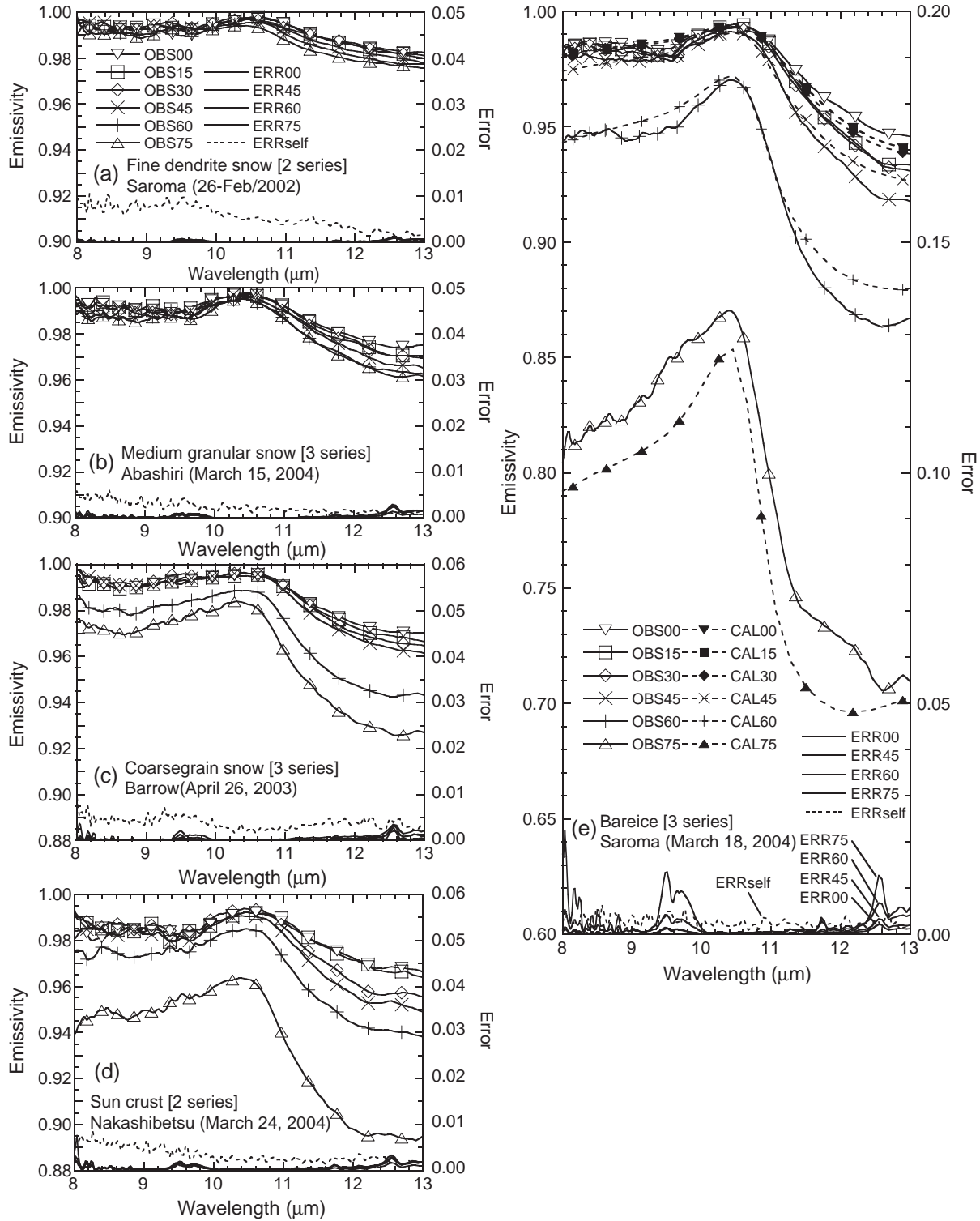


Fig. 8. Directional emissivity spectra at the six exitance angles of 0°, 15°, 30°, 45°, 60°, 75° (OBS00–OBS75) derived for the same surfaces shown in Fig. 7. Fractional emissivity errors due to the uncertainties of the simulated downwelling radiances (ERR00–ERR75) and the temporal drift of the instrument self-emission (ERRself) are shown in the right vertical axis. Also shown only in (e) are the spectra calculated with the Fresnel reflectance theory (CAL00–CAL75). The directional emissivity spectra are averaged over several series of the FT-IR measurements and also averaged every 9 wave number points to smooth the spectrum.

shows the comparison of both studies' results at the exitance angle of 10°. The measured snow grain sizes for each spectrum (median diameter for this study and the range of diameter for Salisbury et al., 1994) are also shown in Fig. 9. The emissivity spectra of snow tend to explicitly reduce in the 11–13 μm

wavelength region with increasing the snow grain size. The spectra for the smooth bare ice from both studies are completely consistent with each other in the spectrally high contrast range in spite of the fact that both studies employed different approaches to derive the emissivity spectra.

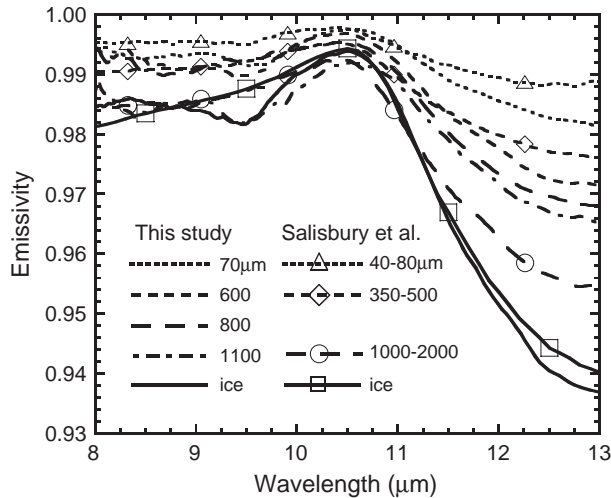


Fig. 9. Emissivity spectra at the exitance angle $\theta_{\text{ext}} = 10^\circ$ measured for various snow types by this study and Salisbury et al. (1994). The spectra of this study are interpolated with those at 0° and 15° . Snow grain sizes observed for the individual spectra are shown as median diameter for this study and as diameter range for Salisbury et al. (1994) both in μm . The spectra by Salisbury et al. (1994) are reproduced from the ASTER Spectral Library (1999).

Because the surface temperature in some snow cases were close to 0°C , the presence of liquid water in the snow is considered here. Although the simulations by Dozier and Warren (1982) show a negligible effect of liquid water on the snow emissivity, the experimental results by Salisbury et al. (1994) show an increase in emissivity in the presence of liquid water leading to a flattening of the reststrahlen band around $\lambda = 12\text{--}13\ \mu\text{m}$. In this study we did not measure the amount of liquid water in the snow. However, from the comparison of the emissivity spectra between this study and Salisbury et al. shown in Fig. 9, we can expect that the effect of liquid water on the derived emissivity is negligibly small in this study. The snow surfaces observed in this study were located under the cold clear sky and thus the loss of longwave radiation can be considered to always keep the ice particles in the infrared skin layer solid.

Salisbury et al. (1994) attributed the cause for the grain size dependence of the snow emissivity to the results of competing processes of the surface and volume scattering. As the grain size increases, the surface scattering is pronounced instead of multiple (volume) scattering which leads to the enhancement of the spectral contrast such as the reflectance peak called the “reststrahlen band”, and vice versa. In particular, the welding process into crust can increase the importance of the surface scattering that has a strong angular dependence. Thus, as the snow grains become welded and closer to a flat smooth ice surface, the snow emissivities are considered to become lower in the reststrahlen band and also exhibit the strong angular dependence.

4.3.2. Angular dependence

The dependence of the snow spectral emissivity on the exitance angle, which has never been examined by laboratory experiments or field measurements, can also be clearly seen in the derived spectra shown in Fig. 8. Fine snow mainly

composed of dendrite crystals (Fig. 8a) exhibits a slight angular dependence indicating that the maximum emissivity difference between the nadir ($\theta_{\text{ext}} = 0^\circ$) and off-nadir angle case ($\theta_{\text{ext}} = 75^\circ$) falls within 0.01. The angular dependence for the medium granular snow (Fig. 8b) is also small with the maximum emissivity variation of about 0.015 at $\lambda = 12.5\ \mu\text{m}$. Both fine and medium snow types observed in this study were more or less composed of disaggregated fine new snow so that the effect of the volume scattering is considered to overwhelm the surface scattering.

The emissivity spectra of the coarse grain snow (Fig. 8c) has a moderate but somewhat discrete dependence on the exitance angle θ_{ext} (the maximum variation exceeds 0.04 at $\lambda = 12.5\ \mu\text{m}$). The angular dependence near the nadir angles ($\theta_{\text{ext}} = 0\text{--}45^\circ$) seems to be comparable to those of the fine and medium granular snow cases, whereas the angular dependence becomes pronounced at the larger angles $\theta_{\text{ext}} = 45\text{--}75^\circ$. The spatial heterogeneity of the snow grain shape observed for this snow (i.e., broken dendrites and coarse ice pellets) can be considered as the cause for the discrete angular dependence of emissivity. That is, the dendrite snow may predominantly contribute to the emissivity property observed at the small exitance angles, while at large angles, the role of the coarse ice pellets possibly becomes pronounced.

The emissivity of sun crust provides a good example for large welded snow grain samples which exhibits strong surface scattering properties, i.e., the strong angular dependence of emissivity. The emissivity spectra of the sun crust (Fig. 8d) explicitly show a continuous reduction from the normal exitance angle ($\theta_{\text{ext}} = 0^\circ$) to the largest angle ($\theta_{\text{ext}} = 75^\circ$) cases. The lowest spectra decrease to around 0.896 at $\lambda = 12.5\ \mu\text{m}$ and $\theta_{\text{ext}} = 75^\circ$ which is the minimum emissivity among the snow samples observed in this study.

The emissivity of the bare ice (Fig. 8e) exhibits the largest angular dependence with the lowest spectra for each angle among the five examined surface types (the minimum reaches down to 0.709 at $\lambda = 12.5\ \mu\text{m}$ and $\theta_{\text{ext}} = 75^\circ$). The spectra are very consistent with the spectra predicted from the Fresnel reflectance theory (CAL00–CAL75 in Fig. 8e) calculated using the complex refractive indices of ice (Warren, 1984). In particular, both are consistent within 0.01 for the near nadir angle cases ($\theta_{\text{ext}} = 0\text{--}45^\circ$). Although the differences between the experimental results and the theory for the $\theta_{\text{ext}} = 60^\circ$ and 75° cases somewhat exceed the accumulated error (0.01) mentioned in Section 4.2.5, these gaps can be considered in part to be due to the small roughness on the ice surface and partly due to calibration error. The small roughness on the ice surface (see Fig. 7e) may act to increase or reduce the effective exitance angles for such large angle cases depending on the effective slope of the surface within the instrument FOV. Thus, the non-ideal surface might lead to the lower and higher emissivity spectra seen for the $\theta_{\text{ext}} = 60^\circ$ and 75° cases, respectively, compared with the spectra calculated with the Fresnel theory in which the ideal flat level surface is assumed. In addition, because the radiance spectra at $\theta_{\text{ext}} = 60^\circ$ and 75° are small and partly beyond the range of warm and cold blackbody spectra (see Fig. 1), the nonlinearity of the FT-IR

detector response could cause some artifacts in the radiance spectra, particularly in the range of $\lambda=11\text{--}13\ \mu\text{m}$ (see the spectrum of L_{GDP} in Fig. 2).

4.3.3. Relationship to the shortwave infrared reflectance

To further validate the observed grain size dependence of the snow emissivity, the derived snow emissivities are compared with the flux reflectances in the SWIR measured by a grating-type spectrometer simultaneously with the FT-IR measurements. In this comparison the reflectances in the TIR are derived from the measured directional emissivity (ϵ) at $\theta_{\text{ext}}=45^\circ$ using Kirchhoff's law given by $\rho(\lambda, -\theta_{\text{ext}}, 2\pi)=1-\epsilon(\lambda, \theta_{\text{ext}})$, where $\rho(\lambda, -\theta_{\text{ext}}, 2\pi)$ is the directional-hemispherical reflectance (DHR) for the wavelength λ at the incidence angle θ_{ext} (Thomas & Stamnes, 1999). The flux reflectance measured with the grating-type spectrometer can also be nearly equalized to $\rho(\lambda, -\theta_{\text{sza}}, 2\pi)$ for the solar zenith angle θ_{sza} in the SWIR wavelength region because the fraction of the diffuse component in the downward solar irradiance is small (typically less than 0.1 under the clear sky in this study) in the SWIR. Although the incidence angle conditions were not strictly the same between the TIR and SWIR reflectance cases, i.e., the solar zenith angle (θ_{sza}) for the SWIR case ranged around $42.9\text{--}60.9^\circ$ contrary to the fixed angle $\theta_{\text{ext}}=45^\circ$ for the TIR cases, we roughly compare the DHRs in both the SWIR and TIR to verify the observed dependence of the TIR snow emissivity upon the snow grain size.

Fig. 10a shows the DHRs in the SWIR ($\rho(1.64\ \mu\text{m}$ and $2.2\ \mu\text{m}$), the left vertical axis) and those in the reststrahlen band in the TIR ($\rho(11\ \mu\text{m}$, $12\ \mu\text{m}$, and $13\ \mu\text{m}$), the right axis) for the four snow types. As the grain size increases, both $\rho(1.64\ \mu\text{m})$ and $\rho(2.2\ \mu\text{m})$ decrease from the maximum of around 0.164 for the fine dendrite snow to the minimum of about 0.034 for the sun crust (the difference between $\rho(1.64\ \mu\text{m})$ and $\rho(2.2\ \mu\text{m})$ is negligibly small less than 0.005.), whereas the DHRs in the TIR increase. An exception is that the DHRs in the SWIR for the coarse grain snow (0.102 at $\lambda=1.64\ \mu\text{m}$ and 0.106 at $\lambda=2.2$

μm) are somewhat larger than those for the medium granular snow (0.082). This can be considered due to the larger solar zenith angle for the coarse grain snow case of about 13° compared with the medium snow case, which has the effect to increase the snow reflectance about 3–4% at those two SWIR wavelengths (Wiscombe & Warren, 1980). The spatial heterogeneity of the snow grain shape seen for the coarse grain snow case mentioned above may also affect the high reflectance of the coarse grain snow. Nevertheless, the DHRs in both the SWIR and TIR have an explicit negative correlation as shown in Fig. 10b. This negative correlation indirectly but explicitly verifies the fact that as the snow grains in the surface shallow layer become coarser, the snow surface becomes more reflective (less emissive) in the reststrahlen bands. Furthermore, the correlation even suggests the possibility of detecting the change in the surface snow type by making use of the spectral contrast of the TIR emissivity (brightness temperature difference) as an alternative to the SWIR reflectance.

4.3.4. Theoretical predictability

The consistency of the grain size dependence of the snow emissivity between this study and Salisbury et al. (1994), and the explicit negative correlation between the SWIR and TIR reflectances shown above, both firmly demonstrate that the scattering process in the TIR occurring in an actual snow layer is not an ideal process predicted solely by the Mie scattering theory employed by Dozier and Warren (1982) which does not show any significant differences of emissivity in the reststrahlen band between the small (diameter: $400\ \mu\text{m}$) and large grain ($2000\ \mu\text{m}$) cases. The simulated directional emissivities with the Mie theory seem to be close only to the fine dendrite snow or medium granular snow cases (Fig. 8a,b) and do not match the other coarser and welded snow cases. This result suggests that the Mie theory fails in simulating the light scattering processes in the TIR in a closely packed and non-spherical particle medium like coarse grain and welded crust snow, in which the independent scattering approximation is

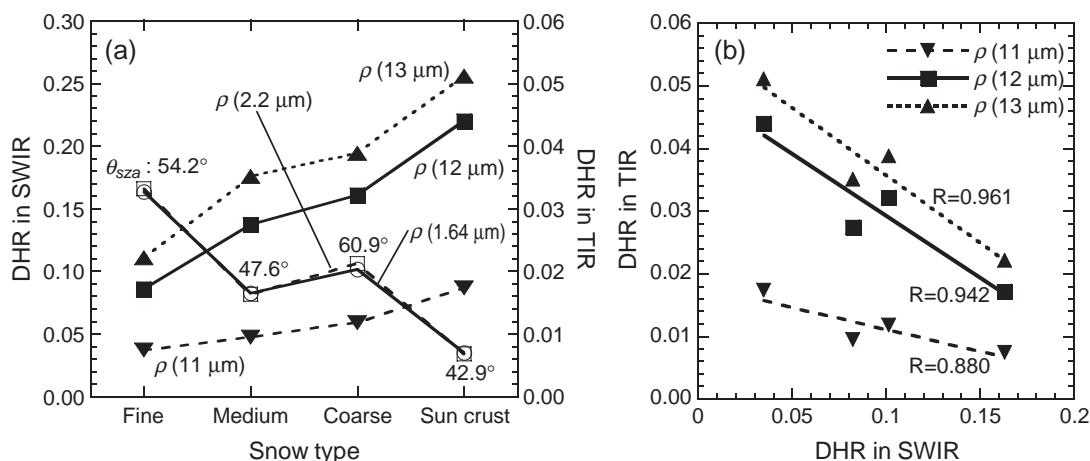


Fig. 10. (a) Comparison of the directional-hemispherical reflectances (DHR) $\rho(\lambda)$ in the TIR at $\lambda=11, 12, 13\ \mu\text{m}$ with those in the SWIR at $\lambda=1.64\ \mu\text{m}$ and $2.2\ \mu\text{m}$ measured for the four snow types (fine dendrite snow, medium granular snow, coarse grain snow, and sun crust), and (b) correlation between the DHRs in the TIR and SWIR (shown only for $\lambda=1.64\ \mu\text{m}$). Solar zenith angle (θ_{sza}) for each SWIR reflectance measurement is shown in (a). The DHRs in the TIR are derived from the measured directional emissivity at the exitance angle $\theta_{\text{ext}}=45^\circ$ using Kirchhoff's law.

considered to be no longer applicable. Our results of the emissivity spectra for the coarse grain snow (Fig. 8c, the median grain diameter is 800 μm) is even smaller than those calculated for the 2000 μm diameter snow using the “diffraction subtraction method” (Fig. 11 of Wald, 1994). The difference exceeds more than 0.02 at the large exitance angles ($\theta_{\text{ext}}=60^\circ$ and 75°). This might suggest that even the diffraction subtraction approximation is not sufficient to simulate the directional emissivity of the disaggregated coarse grain snow. For the prediction of the directional emissivities for the welded snow (Fig. 8d), the weighted sum of the radiative transfer reflectance considering the closely packed effect of the snow medium and the Fresnel reflectance (Wald, 1994) seems to be appropriate to account for the large angular dependence. The weighting should be related to the extent to which the snow grains are welded, which might be able to be assessed by the SWIR reflectance. Further quantitative comparisons between the directional emissivity measurements and those theories proposed for various snow types are desired to be made in the future studies taking into account the effects of snow grain shape, size and the welding of grains in order to make the theoretical prediction of the directional emissivity more accurate.

5. Conclusion

Spectral emissivities of snow and ice surfaces in the TIR are measured by field experiments using a portable FT-IR spectrometer in conjunction with the snow pit work. The dependences of the emissivity on the snow type and exitance angle were examined. The obtained emissivities show distinct spectral features typical for snow and ice surfaces, that is, (1) an emissivity peak at $\lambda=10.5 \mu\text{m}$ due to the locally minimum single scattering albedo (large absorptivity) of the ice particle followed by (2) a broad emissivity trough centered at around $\lambda=12\text{--}13 \mu\text{m}$ due to the surface scattering maximum (reststrahlen band). The spectral contrast seen in the wavelength region from 10.5 to 12.5 μm show an explicit snow type dependence, that is, the emissivity is reduced with increasing the snow grain size. These observed spectral features are quite consistent with those seen in the past laboratory studies.

Another important feature seen in the spectra is the angular dependence. As the exitance angle increases, the emissivities in the high spectral contrast range were only slightly reduced for the disaggregated finer snow cases such as fine dendrite snow and medium granular snow, whereas the emissivities of coarse grain snow and welded sun crust tended to be largely reduced. The emissivity of smooth bare ice, indicating the lowest extreme of emissivity among the studied snow and ice surfaces, exhibited the most significant angular dependence which is successfully predictable with the Fresnel reflectance theory.

The observed dependence of the TIR emissivity (ϵ) on the surface snow type is indirectly supported by the fact that the directional–hemispherical reflectance (DHR) in the TIR calculated by $1-\epsilon$ is negatively well correlated with the measured DHR in the SWIR. In other words, the smaller the snow grains become, the whiter (high reflectivity) in the SWIR

and the blacker (high emissivity) in the TIR the snow surface becomes, and vice versa. The close correlation between the TIR emissivity and SWIR reflectance even suggests the possibility to detect the change in the surface snow type by examining the brightness temperature difference in the TIR as an alternative to the SWIR reflectance.

The spectral contrasts in the TIR observed for coarse grain snow and welded sun crust cases are too strong to be accounted for solely by the scattering process based on the Mie theory. The directional emissivity of coarse and welded snow should be derived by the combined theory of the radiative transfer theory and the Fresnel reflectance theory taking into account the extent to which the snow grains are welded as proposed by Wald (1994).

Our results clearly indicate that the brightness temperatures of snow/ice surfaces in the TIR can deviate from their true physical temperatures depending on the snow type. In addition, the deviation can be significantly pronounced with increasing the exitance angle particularly for the coarse and welded snow or smooth bare ice cases, as opposed to the fine and medium grain snow cases, which is the fact verified for the first time by this in-situ measurement study. Because the strongest and the most variable spectral contrast of emissivity occurs at around $\lambda=11\text{--}12 \mu\text{m}$ where the TIR spectral bands of satellite sensors are commonly located, it is important to select the appropriate emissivity for the accurate retrieval of surface temperatures and also for the nighttime cloud detection over cold snow/ice surfaces needed for radiation budget studies. The observed variations of snow and ice emissivities also suggest that the discrimination between snow/ice types at the surface such as fine new snow, coarse snow, welded snow, and smooth ice from space might be possible using only TIR radiances.

For the last application, at least three unknown factors have to be known, i.e., the physical temperature of the surface, the effects of atmospheric absorption and emission on the TIR radiances at the top of the atmosphere, and the topography in order to isolate the emissivity variation as a function of viewing angle. Also needed to be considered is the mixed pixel problem which is a general inevitable problem for the remote sensing study (e.g., Becker et al., 1981) but not detailed here. By virtue of the low water vapor content in the cryosphere in winter season and the relatively high snow emissivity of around 0.99 (0.98 for bare ice) at $\lambda=11 \mu\text{m}$ at the exitance angle range of $0\text{--}45^\circ$ corresponding to the viewing angle range of common satellite sensors, the physical temperature of the snow surface can be roughly estimated solely from the brightness temperature at 11 μm band. Then, the emissivity variation can be determined from the brightness temperature (or radiance) difference between 11 μm and 12 μm bands by taking into account the effective slope of the ground surface. Probably the bare ice area seen in the Antarctic ice sheet where the content of water vapor is very low and the surface slope is gentle or negligibly small can be successfully identified with the TIR emissivity variation, whereas the discrimination between snow types over mountainous area in the melting season is expected to suffer from both the water vapor absorption and the complicated topographic effects. As the next step, it will be

necessary to examine the possibility to discriminate between the surface snow types from space with the TIR emissivity variation by applying the derived directional emissivity spectra to the analysis of actual satellite datasets taking into account those factors mentioned above.

Acknowledgements

This work was conducted as part of the ADEOS-II/GLI Ca/Val experiment supported by Japan Aerospace Exploration Agency (JAXA). The authors would like to thank the cooperation of the U.S. Department of Energy as part of the Atmospheric Radiation Measurement Program for the use of the atmospheric radiation data and the ARM facilities at the North Slope of Alaska site. Atmospheric profiles (JMAOA) data were provided by Japan Meteorological Agency. We thank Yasuko Iizuka for obtaining some of snow pit work results used in this paper and many helpful comments. We are also grateful to the three anonymous reviewers, and their useful comments and suggestions on the original manuscript. M.H. conceived and designed the experiment, and together with R.S. and F.T. carried out the measurements and data analysis of snow TIR emissivity; T.A. and T.T. together with H.M. and H.E. carried out the measurements and data analysis of snow SWIR reflectance; A.H., K.S., and T.J.Y. together with Y.N. designed and carried out the snow pit work; M.H. wrote the paper.

References

- Aoki, T., Aoki, T., Fukabori, M., Hachikubo, A., Tachibana, Y., & Nishio, F. (2000). Effects of snow physical parameters on spectral albedo and bidirectional reflectance of snow surface. *Journal of Geophysical Research*, *105*, 10219–10236.
- ASTER Spectral Library (1999). Reproduced from the ASTER Spectral Library through the courtesy of the Jet Propulsion Laboratory, California Institute of Technology, Pasadena, California. Copyright © 1999, California Institute of Technology. ALL RIGHTS RESERVED <http://speclib.jpl.nasa.gov/>
- Becker, F., Ngai, W., & Stoll, M. P. (1981). An active method for measuring thermal infrared effective emissivities: Implications and perspectives for remote sensing. *Advances in Space Research*, *1*, 193–210.
- Beer, R., Glavich, T. A., & Rider, D. M. (2001). Tropospheric emission spectrometer for the earth observing system's aura satellite. *Applied Optics*, *40*, 2356–2367.
- Berger, R. H. (1979). Snowpack optical properties in the infrared. *CRREL Rep.*, vol. 79 (pp. 11). Hanover, New Hampshire: U. S. Army Cold Regions Research and Engineering Laboratory.
- Berk, A., Bernstein, L., Anderson, G., Acharya, P., Robertson, D., Chetwynd, J., et al. (1998). MODTRAN cloud and multiple scattering upgrades with application to AVIRIS. *Remote Sensing of Environment*, *65*, 367–375.
- Clerbaux, C., Hadji-Lazarou, J., Payan, S., Camy-Peyret, C., Wang, J., Edwards, D. P., et al. (2002). Retrieval of CO from nadir remote-sensing measurements in the infrared using four different inversion algorithms. *Applied Optics*, *41*, 7068–7078.
- Colbeck, S. C., Akitaya, E., Armstrong, R., Gubler, H., Lefeulle, J., Lied, K., et al. (1990). The international classification for seasonal snow on the ground. Wallingford, Oxfordshire: International Association of Hydrological Sciences, International Commission on Snow and Ice.
- Demirgian, J., & Dedecker, R. (2005). Atmospheric Emitted Radiance Interferometer (AERI) handbook. ARMTR-054. http://www.arm.gov/publications/tech_reports/handbooks/
- Dozier, J., & Warren, S. G. (1982). Effect of viewing angle on the infrared brightness temperature of snow. *Water Resources Research*, *18*, 1424–1434.
- Japanese Society of Snow and Ice. (1998). JSSI classification for snow cover. *Journal of the Japanese Society of Snow and Ice*, *60*, 419–436.
- Key, J., & Haefliger, M. (1992). Arctic ice surface temperature retrieval from AVHRR thermal channels. *Journal of Geophysical Research*, *97*, 5885–5893.
- Key, J. R., Collins, J. B., Fowler, C., & Stone, R. S. (1997). High-latitude surface temperature estimates from thermal satellite data. *Remote Sensing of Environment*, *61*, 302–309.
- Knuteson, K. O., Revercomb, H. E., Best, F. A., Ciganovich, N. C., Dedecker, R. G., Dirks, T. P., et al. (2004a). Atmospheric emitted radiance interferometer. Part I: Instrument design. *Journal of Atmospheric and Ocean Technology*, *21*, 1763–1776.
- Knuteson, K. O., Revercomb, H. E., Best, F. A., Ciganovich, N. C., Dedecker, R. G., Dirks, T. P., et al. (2004b). Atmospheric emitted radiance interferometer. Part II: Instrument performance. *Journal of Atmospheric and Ocean Technology*, *21*, 1777–1789.
- Korb, A. R., Dybwad, P., Wadsworth, W., & Salisbury, J. W. (1996). Portable FTIR spectrometer for field measurements of radiance and emissivity. *Applied Optics*, *35*, 1679–1692.
- Korb, A. R., Salisbury, J. W., & D'Aria, D. M. (1999). Thermal-infrared remote sensing and Kirchhoff's law 2. Field measurements. *Journal of Geophysical Research*, *104*, 15339–15350.
- Li, W., Stammes, K., Chen, B., & Xiong, X. (2001). Snow grain size retrieved from near-infrared radiances at multiple wavelengths. *Geophysical Research Letters*, *28*, 1699–1702.
- Liu, Y., Key, J. R., Frey, R. A., Ackerman, S. A., & Menzel, W. P. (2004). Nighttime polar cloud detection with MODIS. *Remote Sensing of Environment*, *92*, 181–194.
- Ozeki, T., & Akitaya, E. (1996). Field observations of sun crust formation in Hokkaido. *Japan. Arctic and Alpine Research*, *28*, 244–248.
- Salisbury, J. W., D'Aria, D. M., & Wald, A. (1994). Measurements of thermal infrared spectral reflectance of frost, snow, and ice. *Journal of Geophysical Research*, *99*, 24235–24240.
- Snyder, W. C., Wan, Z., Zhang, Y., & Feng, Y.-Z. (1998). Classification-based emissivity for land surface temperature measurement from space. *International Journal of Remote Sensing*, *19*, 2753–2774.
- Thomas, G. E., & Stammes, K. (1999). *Radiative transfer in the atmosphere and ocean*. New York: Cambridge University Press.
- Wald, A. (1994). Modeling thermal infrared (2–14 μm) reflectance spectra of frost and snow. *Journal of Geophysical Research*, *99*, 24241–24250.
- Wan, Z. (1999). MODIS land-surface temperature algorithm theoretical basis document (LST ATBD). Version 3.3, Contract Number: NAS5-31370. pp. 77. An electronic file is available at the following URL (http://modis.gsfc.nasa.gov/data/atbd/atbd_mod11.pdf)
- Wan, Z., Zhang, T. (1999). *MODIS UCSB Emissivity Library*. <http://www.icess.ucsb.edu/modis/EMIS/html/em.html>
- Wan, Z., Zhang, Y., Ma, X., King, M. D., Myers, J. S., & Li, X. (1999). Vicarious calibration of the moderate-resolution imaging spectroradiometer airborne simulator thermal-infrared channels. *Applied Optics*, *38*, 6294–6306.
- Warren, S. G. (1982). Optical properties of snow. *Reviews of Geophysics and Space Physics*, *20*, 67–89.
- Warren, S. G. (1984). Optical constants of ice from the ultraviolet to the microwave. *Applied Optics*, *23*, 1206–1225.
- Wiscombe, W. J., & Warren, S. G. (1980). A model for the spectral albedo of snow. I: Pure snow. *Journal of Atmospheric Science*, *37*, 2712–2733.
- Yamanouchi, T., Suzuki, K., & Kawaguchi, S. (1987). Detection of clouds in Antarctica from infrared multispectral data of AVHRR. *Journal of Meteorological Society of Japan*, *65*, 949–962.